Colloids and Surfaces A: Physicochemical and Engineering Aspects 648 (2022) 129233

Contents lists available at ScienceDirect

Colloids and Surfaces A: Physicochemical and Engineering Aspects

journal homepage: www.elsevier.com/locate/colsurfa

Ag nanoparticle-decorated Bi_2O_3-TiO_2 heterogeneous nanotubular photocatalysts for enhanced degradation of organic contaminants

Yan Wang [a], Shengzhe Zhao [a], Yi Yang [a], Raul D. Rodriguez [b], Anya Lipovka [b], Yun Lu [c,*], Honglan Huang [a,b,c], Jinju Chen [a,*]

[a] School of Materials and Energy, University of Electronic Science and Technology of China, Chengdu 610054, PR China
[b] Tomsk Polytechnic University, Lenina Ave. 30, 634034 Tomsk, Russia
[c] School of Electronic Science and Engineering, University of Electronic Science and Technology of China, Chengdu 610054, PR China

HIGHLIGHTS

- Ag@Bi_2O_3-TiO_2 nanostructures were obtained by combining sacrificial templates and photoreduction.
- The photocatalysts exhibited enhanced photodegradation for RhB and TCH.
- The LSPR excitation of Ag on Bi_2O_3-TiO_2 promoted visible light absorption.
- The photocatalysts has stable recyclability for actual application.

GRAPHICAL ABSTRACT

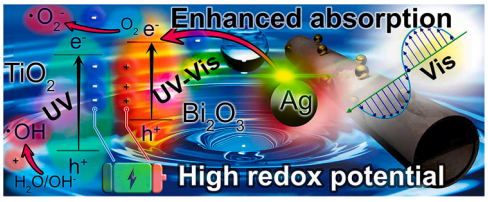

ARTICLE INFO

Keywords:
Ag nanoparticles
Bi_2O_3-TiO_2 heterostructure
Photodegradation
Organic contaminants

ABSTRACT

Ag nanoparticle-decorated Bi_2O_3-TiO_2 heterogeneous photocatalysts were successfully obtained by combining facile sacrificial templates and photoreduction. The as-synthesized Ag@Bi_2O_3-TiO_2 photocatalysts with a narrow band gap of 2.40 eV exhibited considerable photocatalytic activity to degrade rhodamine B (RhB) and tetracycline hydrochloride (TCH), and the removal efficiency reached 100% and 92%, respectively. Ag@Bi_2O_3-TiO_2 photocatalysts also exhibited stable recyclability for the degradation of RhB and TCH. Trapping experiments helped determine the major reactive oxidative species for TCH photodegradation. The desirable photodegradation performance is mainly attributed to improved light absorption, enhanced charge separation, and strong redox capacity of Ag@Bi_2O_3-TiO_2 nanostructures with S-scheme heterojunction. This work provides a facile avenue to construct heterogeneous tubular nanostructures with intensive photoabsorbance and effective photocatalysis to degrade organic contaminants.

1. Introduction

Organic contaminants in aquatic ecosystems have caused severe damage to the environment due to the high toxicity and difficult biodegradation, posing a threat to socially sustainable development [1]. One of the primary sources of contaminants is the synthetic dye wastewater discharged from textiles, foodstuffs, and leather industries [2]. Generally, even a low concentration of dye solution (10 mg/L or lower) can reduce the light transmittance of water environment and destroy the photosynthesis of aquatic ecosystem. Also, once exposed to and into the body by organisms, aromatic amines can be generated through biological metabolism, which has potent carcinogenicity and environmental persistence [3,4,5]. Another contaminant source is from the abundant use of antibiotics [6]. The overuse of antibiotics can

* Corresponding authors.
E-mail addresses: luyun1501@163.com (Y. Lu), jinjuchen@uestc.edu.cn (J. Chen).

https://doi.org/10.1016/j.colsurfa.2022.129233
Received 9 March 2022; Received in revised form 3 May 2022; Accepted 11 May 2022
Available online 16 May 2022

disrupt the gut flora of humans, leading to inflammatory responses and poor responses to flu vaccines [7]. Among them, tetracyclines are widely applied as broad-spectrum bacteriostasis with their metabolites that have been detected in various aquatic environments. Tetracycline residues in the environment decrease microbial diversity and promote the development and evolution of antibiotic-resistant microorganisms [8,9]. This issue may pose a potential threat to human drinking and irrigation water, which thus affects human health and harms the ecological balance. Technically, removing refractory organic pollutants by traditional treatment methods (adsorption [10], biodegradation [11], flocculation precipitation [12], and catalytic wet oxidation [13]) have some inevitable problems, such as high cost and secondary pollution, which is difficult to achieve ideal treatment effect. To entirely remove organic pollutants to minimize contamination risks, photocatalysis is usually considered an effective method with advantages of low cost, environmental friendship, and sustainability.

It has been studied for several decades and substantial progress has been made in some important research subjects from photocatalytic material design [14] to applications in environment purification [15]. Titanium dioxide (TiO_2), a multifunctional semiconductor metal oxide, is a widely used and promising candidate for photocatalytic degradation due to its unique optical, electronic, and photoactive properties [16,17,18]. However, some crucial restrictive factors hinder its practical application in the industrial community, including the high recombination rate of photogenerated electron-hole pairs and the low solar energy conversion efficiency due to its wide band gap [19]. The construction of heterostructure is a neat way to solve these problems simultaneously. For instance, S-scheme heterojunction can achieve the spatial separation of redox reaction sites and retain the strong redox capacity of carriers. Moreover, the spectral response range can be broadened by compositing with the narrow band gap semiconductor [20,21]. Moreover, suitable nanostructures are engineered to increase active sites and photocatalytic activity for enhanced degradation, such as nanosheets [22], nanoflowers [23], quantum dots loaded on nanosheets [24], nanotubes [25], etc. Bismuth oxide (Bi_2O_3) has a good photosensitizing effect, and its band gap varies from 2 eV to 3.96 eV due to different phase compositions of monoclinic, tetragonal, hexagonal, and cubic phases [26,27,28,29]. Narrow band gap Bi_2O_3 appears as a promising candidate to form a heterojunction with TiO_2 to boost photocatalytic performance. Recently, Bi_2O_3-TiO_2 composites were synthesized by using different methods for the removal of organic contaminants and their photocatalytic activity was enhanced to some extent compared with that of TiO_2 alone [20,21,30,33]. However, the synthetic route requires a multistep process and a long time for most reported photocatalysts, including Bi_2O_3/TiO_2 film [19], Bi_2O_3/TiO_2 hierarchical heterostructure [20], Bi_2O_3/TiO_2 porous nanostructures [32], and Bi_2O_3/TiO_2 nanoparticles [34]. So the synthesis of Bi_2O_3-TiO_2 heterogeneous photocatalysts with high performance using a simple strategy remains an exciting challenge.

Photo-assisted catalysis mediated by localized surface plasmon resonance (LSPR) of nanometals has become a frontier research field of solar-to-chemical-energy conversion in recent years [35,36]. Plasmonic nanometals can effectively combine light-harvesting, hot-electron generation, and unique catalytic activity in a compound material where nanometals act as cocatalysts [15,20]. Ag nanoparticles (Ag NPs) modified semiconductors exhibited improved photocatalytic performance in previous studies [37,38]. Therefore, it is of considerable interest to construct Ag NPs-modified Bi_2O_3-TiO_2 heterogeneous nanotubular photocatalysts for the efficient removal of organic pollutants from water.

In this work, we present a facile process for fabricating Ag@Bi_2O_3-TiO_2 heterogeneous nanotubular photocatalysts by combing sacrificial templates with photoreduction. Bi_2O_3 and Ag nanoparticles were homogeneously distributed on nanotubular TiO_2 to provide high-density of active sites. S-scheme Bi_2O_3-TiO_2 heterojunction ensured that the electrons in Bi_2O_3 and the holes in TiO_2 were spatially separated with strong redox ability. Furthermore, the LSPR of Ag NPs made the heterostructures exhibit strong spectral absorption in the visible spectral range and thus produce more effective photocarriers. High photocatalytic degradation activities of the as-prepared Ag@Bi_2O_3-TiO_2 photocatalysts for rhodamine B (RhB) and tetracycline hydrochloride (TCH) were observed under full-spectrum light irradiation. Moreover, the possible S-scheme heterojunction photocatalytic mechanism for the degradation of pollutants was discussed in this paper.

2. Experimental

2.1. Materials

N,N-dimethylformamide (DMF) was obtained from Aladdin. Bismuth (III) neodecanoate (BN) was purchased from Sigma-Aldrich. Tetrabutyl titanate (TBOT) and tetracycline hydrochloride (TCH) were supplied by Shanghai Macklin Biochemical Co., Ltd. Rhodamine B (RhB) and absolute ethanol were purchased from Chengdu Jinshan Chemical Reagent Co., Ltd. $AgNO_3$ was obtained from Sinopharm Chemical Reagent Co., Ltd. Polyacrylonitrile (PAN, Mw=85,000) was purchased from Shanghai D&B Biological Science and Technology Co., Ltd. Ethanol (EA), ethylenediaminetetraacetic acid disodium salt (EDTA-2Na), p-Benzoquinone (P-BQ), and t-butanol (TBA) were supplied by Chengdu Chron Chemicals Co., Ltd. All chemicals were of analytical reagent grade and used without further purification.

2.2. Preparation of Ag@Bi_2O_3-TiO_2 photocatalysts

Ag@Bi_2O_3-TiO_2 photocatalysts were prepared using sacrificial templates (PAN fibers) combined with photoreduction (as shown in Scheme 1). To prepare the spinning solution, a proper PAN was dissolved in DMF. The solution was loaded into a syringe connected to a positive electrode of a high-voltage power supply. The flow rate of the solution was controlled at 0.5 mL h^{-1}. A 20 cm work distance between the tip and the rotating collector and 16 kV voltage were used during electrospinning. The humidity was kept below 30% during the preparation. For the first step, the PAN fibers were soaked in TBOT/EA precursor solution for 15 min, in which the volume ratio of TBOT to EA was 1:10. After complete infiltration, the TBOT/PAN fibers were dried at 60 °C. Secondly, the heat-treated TBOT/PAN fibers (precursor fibers) were obtained at 210 °C for 4 h in an oven, and then immersed in BN/EA solution with different concentrations of 0.25, 0.5, and 1 g/10 mL. Thirdly, the BN/TBOT/PAN samples were calcined at 550 °C for 2 h at a heating rate of 5 °C min^{-1}. Bi_2O_3-TiO_2 heterostructures with different content of Bi_2O_3 were obtained after finishing the calcination process. These as-prepared samples were labeled TB1, TB2, and TB3, respectively. Finally, with a typical photo-reduction procedure, TB2 was placed in a 0.2 M $AgNO_3$ solution with magnetic stirring in the dark for 1 h to ensure the well mixing of solution and sample. Subsequently, the mixture was subjected to full-spectrum light irradiation for 20 min. After centrifugal cleaning and drying, Ag@Bi_2O_3-TiO_2 photocatalysts were obtained and named ATB2. Pure TiO_2 nanotubes were obtained by calcinating precursor fibers without additional steps.

2.3. Characterization

The morphologies of the as-prepared nanotubes were observed by scanning electron microscopy (SEM, Helios G4 UC, Thermo Fisher Scientific) equipped with energy dispersive X-ray analysis (EDX, Aztec Live ULTIM, Oxford Instruments) and transmission electron microscopy (TEM, Tecnai G^2 F20 S-TWIN, Thermo Fisher Scientific). Information on the phases and purity of the samples was obtained by X-ray powder diffraction measured on a SmartLab-9 kW diffractometer (XRD, Rigaku, Japan) using Cu Kα radiation ($\lambda = 0.15418$ nm) under 40 kV and 30 mA, within a scanning range from 5° to 80°. X-ray photoelectron spectroscopy was performed using AXIS Ultra DLD (XPS, Kratos), and C 1s peak

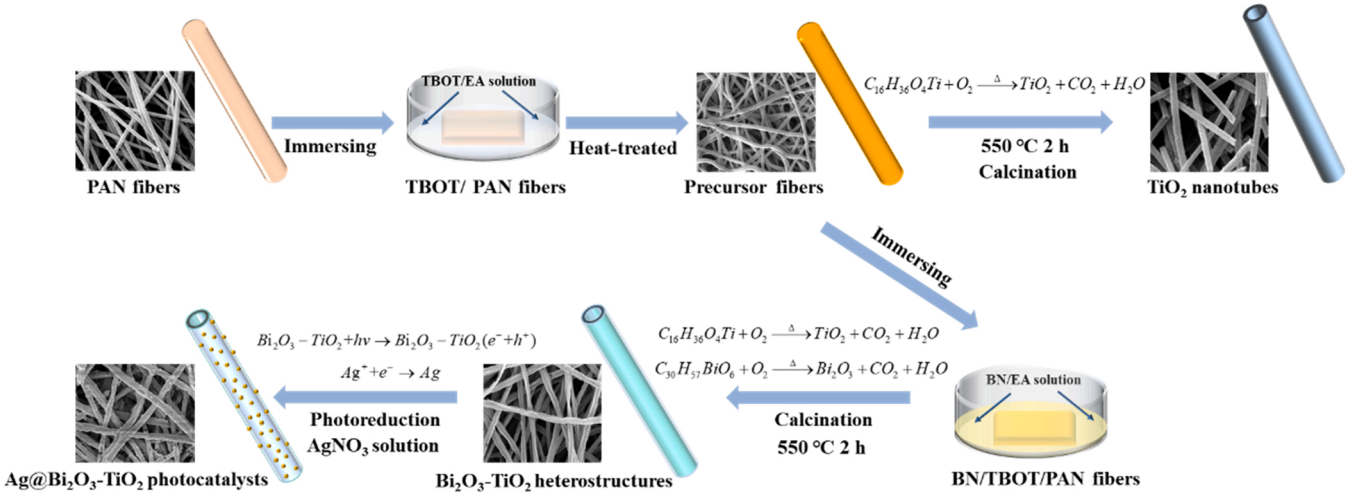

Scheme 1. An illustration of the formation of Ag@Bi_2O_3-TiO_2 photocatalysts.

(284.6 eV) was used for reference. UV-Vis spectra were recorded on a UV–vis spectrophotometer (UV-2550, Shimadzu) with a scanning range from 200 to 800 nm. Fluorescence spectrophotometer (F7000, Hitachi) was used for the photoluminescence (PL) measurements with an excitation of 325 nm. The prepared photocatalysts films were used as the working electrode, meanwhile, a platinum foil as the counter electrode and a 3 M KCl Ag/AgCl electrode as the reference electrode. The electrochemical impedance spectroscopy (EIS) and Mott-Schottky

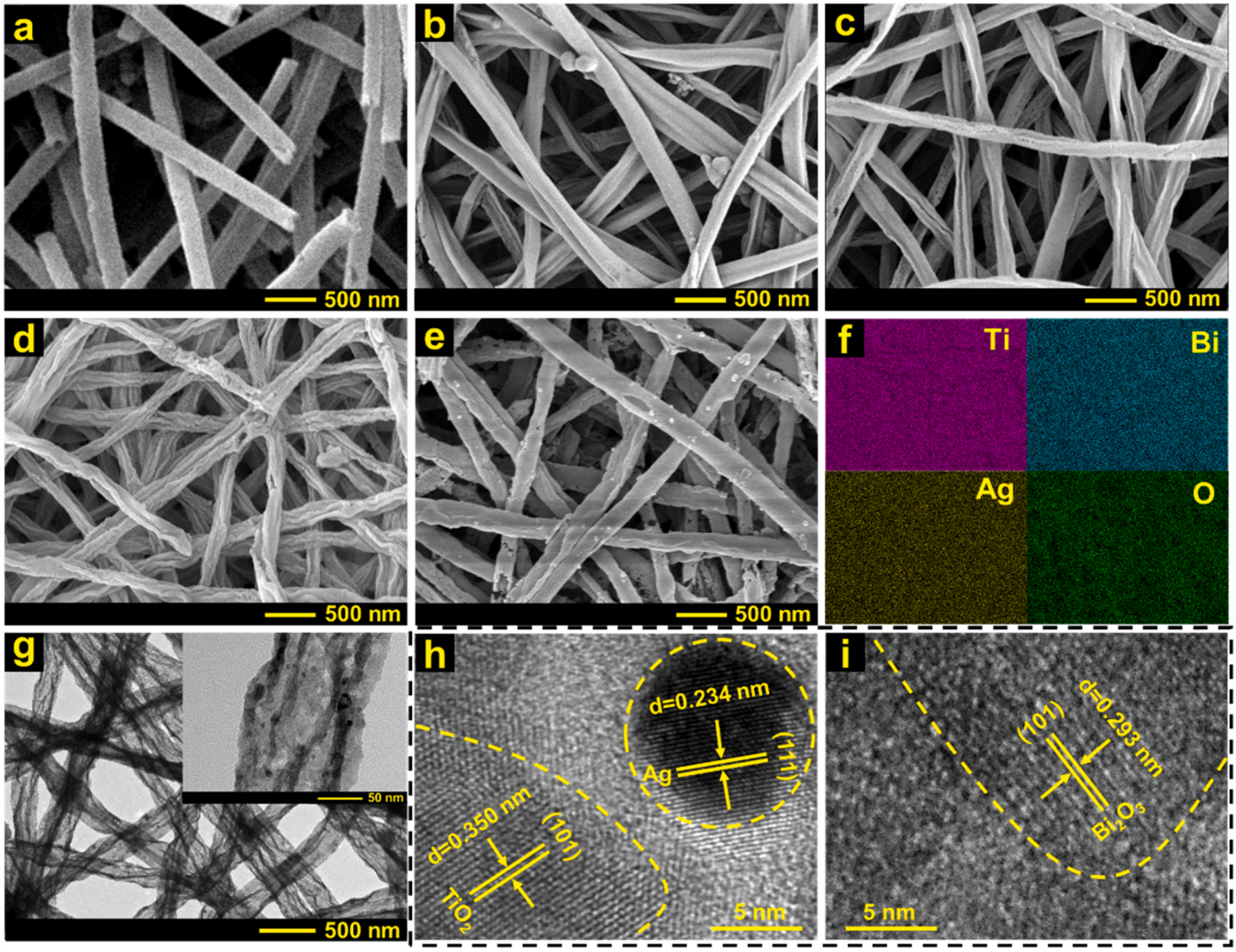

Fig. 1. SEM images of the as-prepared samples: (a) TiO_2 nanotubes, (b–d) TB1-TB3 heterostructures, and (e) ATB2 photocatalysts. (f) EDX mapping of ATB2 photocatalysts. (g) TEM and (h, i) HRTEM images of ATB2 photocatalysts.

curves were measured by with an electrochemical workstation (Chenhua CHI660E, Shanghai). The degradation process was monitored using UV-Vis spectrophotometry, measuring the absorption of RhB at 546 nm and TCH at 357 nm.

2.4. Photocatalytic evaluation

RhB has been vastly used as a model compound to evaluate photocatalytic activity, primarily attributed to its frequent occurrence in industrial waste discharge. Photocatalytic activity of the samples was evaluated by degradation of aqueous RhB under full-spectrum light irradiation. First, an aqueous solution of RhB (20 mL, 10 mg/L) was placed in a quartz tube and 20 mg of the samples were added. Then, the dispersion was magnetically stirred in the dark for 2 h to ensure adsorption-desorption equilibrium between the RhB dye and the as-prepared samples. Afterward, the dispersion was exposed to a xenon lamp (300 W) for photocatalytic degradation. At given time intervals, 2 mL of the suspension was taken out and centrifuged to remove the photocatalyst particles. The degradation efficiency of RhB was monitored by comparing the characteristic absorption intensity of RhB at 546 nm at different times and compare with that of the original RhB.

The photocatalytic performances of the obtained samples were also investigated using 50 mg/L TCH as a pollutant model. In the same way, the xenon lamp (300 W) was used as the light source. Briefly, 20 mg photocatalysts was dispersed into 20 mL of TCH solution. Similarly, the suspension was magnetically stirred in the dark to establish the

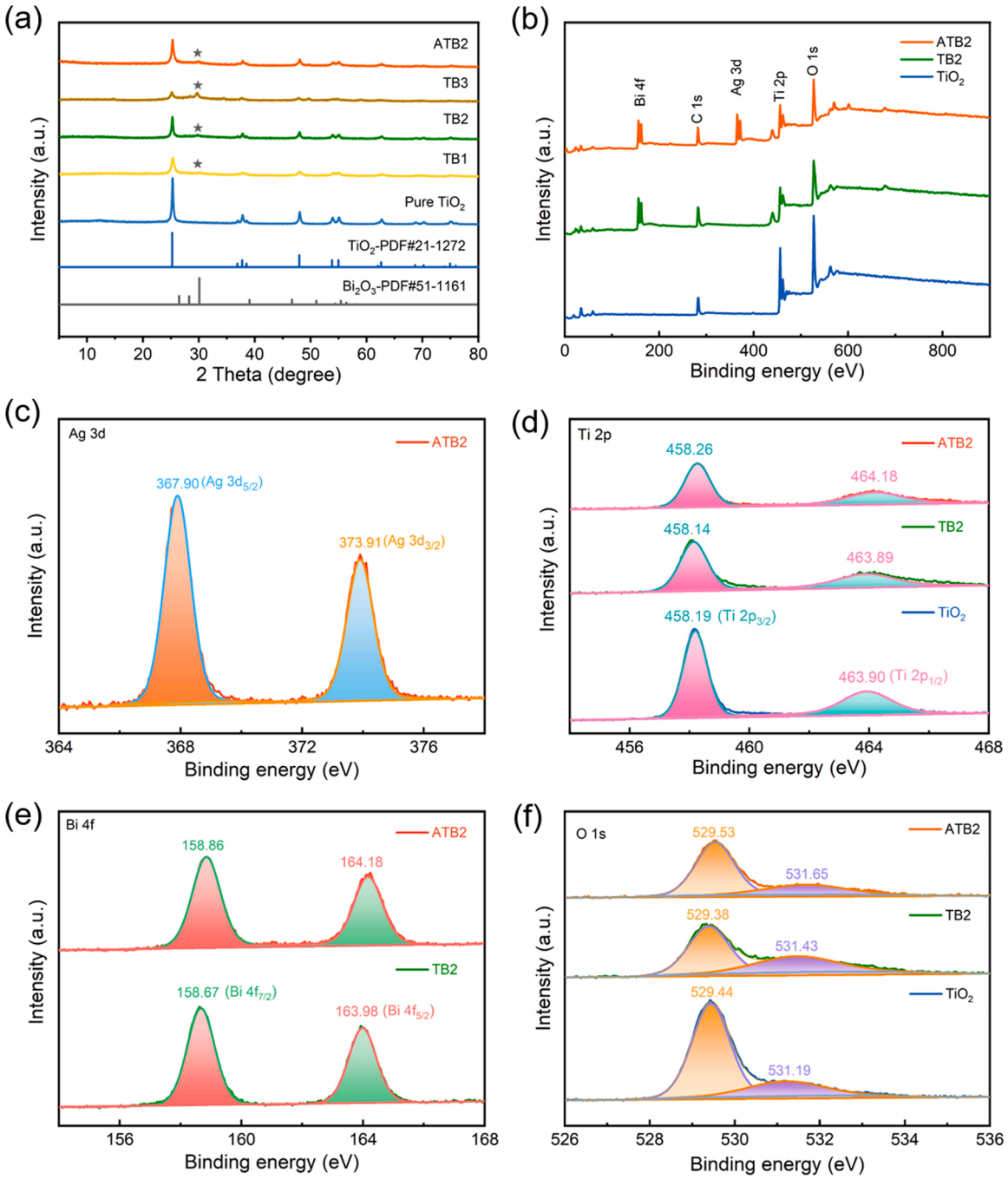

Fig. 2. (a) XRD patterns of TiO_2 nanotubes, TB1-TB3 heterostructures, and ATB2 photocatalysts. (b) The full XPS spectra of TiO_2, TB2, and ATB2 photocatalysts. High resolution XPS spectra of (c) Ag 3d, (d) Ti 2p, (e) Bi 4f, and (f) O 1s.

adsorption-desorption equilibrium. At a specific time interval, 1 mL suspension was taken out and centrifuged to remove the photocatalyst particles. The concentrations of TCH were analyzed by absorption spectroscopy at the characteristic absorption peak of 357 nm.

3. Results and discussion

The morphologies of PAN fibers, TiO_2 nanotubes, TB1-TB3 heterostructures, and ATB2 photocatalysts were investigated by SEM and TEM. As shown in Fig. 1(a), the as-prepared TiO_2 nanotubes are even via the PAN sacrificial templates (Fig S1(a, b) in the Supporting Information (SI)) and the hollow structure of TiO_2 nanotubes can be roughly observed from the broken part of the nanotubes. Pure Bi_2O_3 is observed to be a lamellar structure after removing the sacrificial templates, as shown in Fig. S1(c, d) in SI. The TB1 to TB3 heterostructures morphologies are shown in Fig. 1(b–d), respectively. Compared with TiO_2 in Fig. 1(a), the introduction of Bi_2O_3 makes the surface of nanotubes wrinkle at different degrees due to the growing internal stress during Bi_2O_3 crystallization. Intact foldable structures of TB2 are shown in Fig. 1(c), with an increased number of active sites for photocatalytic reaction. As shown in Fig. 1(e), to some extent, the morphology of ATB2 photocatalysts changes due to the deposition of Ag on the surface of TB2 heterostructures. The EDX mapping in Fig. 1(f) proves that Ti, Bi, O, and Ag are present in the ATB2 photocatalysts. The TEM image of ATB2 photocatalysts (Fig. 1(g)) further confirms that the nanotubes are uniform in size and super small-sized Ag nanoparticles are successfully combined with Bi_2O_3-TiO_2 nanotubes. HRTEM images of the enlarged illustration in Fig. 1(g) are shown in Fig. 1(h, i). As can be seen in Fig. 1 (h, i), the lattice fringes show interplanar distances of 0.350, 0.234, and 0.293 nm, corresponding to the (101) planes of anatase TiO_2, (111) planes of cubic Ag, and (101) planes of hexagonal Bi_2O_3, respectively. All these results confirm that the Ag@Bi_2O_3-TiO_2 photocatalysts are successfully obtained.

XRD results of pure TiO_2, TB1, TB2, TB3, ATB2, and pure Bi_2O_3 are presented in Fig. 2(a) and Fig. S2(a) in SI, respectively. Pure TiO_2 has strong diffraction peaks at 25.3°, 37.8°, 48.0°, 53.9°, 55.1°, and 62.7°, corresponding to (101), (004), (200), (105), (211), and (204) of anatase TiO_2, respectively (JCPDS NO. 21-1272). All diffraction peaks of TiO_2 are also observed in TB1-TB3, but the diffraction peak intensity is lower than that of pure TiO_2, indicating that the addition of Bi_2O_3 inhibits the growth of TiO_2 grain. There is no noticeable shift in the diffraction peaks of TiO_2, indicating that Bi_2O_3 exists as a separate phase rather than being incorporated into TiO_2 lattice. There is one additional diffraction peak at 30.14° in the XRD pattern of TB1-TB3, which is assigned to the (101) crystal plane of hexagonal Bi_2O_3 phase (JCPDS NO. 51-1161). Furthermore, the intensity of the diffraction peak strengthens with the increase of Bi_2O_3 content. The diffraction spectrum of ATB2 shows the same trend as that of TB2. Ag diffraction peaks are not observed due to the tiny amount shown in the EDX spectrum (Fig. S2(b) in SI).

XPS is used to measure the chemical composition and bonding energy of the as-prepared photocatalysts. The full survey spectrum of the ATB2 sample in Fig. 2(b) includes characteristic peaks of Ti 2p, Bi 4f, O 1s, and Ag 3d, indicating the coexistence of Ti, Bi, O, and Ag elements. This fairly agrees with EDX elemental analysis (Fig. S2(b) in SI). In the high-resolution spectrum of Ag 3d (Fig. 2(c)), the symmetrical peaks at 367.90 eV and 373.91 eV can be ascribed to the Ag $3d_{5/2}$ and Ag $3d_{3/2}$, respectively. The spin separation energy of the Ag 3d doublet is 6.01 eV, showing that Ag is in its metallic state [37,38,39,40]. The characteristic peak of Ag $3d_{5/2}$ shifts to the lower binding energy compared with the corresponding value of pure metallic Ag due to the interaction between Ag and semiconductors (the standard binding energy of Ag $3d_{5/2}$ for bulk Ag is about 368.20 eV [41]). For pure TiO_2, peaks with binding energies of 458.19 eV and 463.90 eV are indexed to Ti $2p_{3/2}$ and Ti $2p_{1/2}$ (Fig. 2(d)), respectively. The splitting energy between Ti $2p_{3/2}$ and Ti $2p_{1/2}$ is 5.71 eV, which is related to Ti^{4+} oxidation state, implying the presence of Ti-O bonds [37,42,43,44]. After the formation of ATB2, the binding energy of Ti 2p shifts higher position, indicating that electrons of Ti would transfer to Ag attributed to the mutual effect between Ag and TiO_2. In terms of high-resolution spectrum of Bi 4f in Fig. 2(e), peaks located at 158.86 eV and 164.18 eV are indexed to Bi $4f_{7/2}$ and Bi $4f_{5/2}$. Notably, the splitting energy between Bi $4f_{7/2}$ and Bi $4f_{5/2}$ is 5.31 eV, confirming the formation of Bi_2O_3 [20,34,45]. A positive shift of Bi 4f is observed in ATB2 compared with that of TB2, also revealing the interaction between Ag and semiconductors. As seen in Fig. 2(f), O 1s spectra of TiO_2, TB2, and ATB2 can be all divided into two spin-orbit components. In addition to the surface adsorbed oxygen corresponding to the higher binding energies, the crystal lattice oxygen atoms of TiO_2, TB2 and ATB2 are located at 529.44, 529.38, and 529.53 eV, respectively [34,35,42]. Compared with that of TiO_2 and TB2, the O 1s peaks of ATB2 shift to higher binding energy, indicating that the electrons are transferred from semiconductors to Ag NPs, which can improve the interaction between the different phases of the photocatalysts [21]. The detailed binding energies and splitting energies of Ag 3d, Ti 2p, Bi 4f and O 1s are shown in Table S1.

The optical absorption properties of the prepared TiO_2 nanotubes, TB2 heterostructures, and ATB2 photocatalysts are determined by UV-Vis diffuse reflectance spectra. As shown in Fig. 3(a), the absorption edge of TiO_2 nanotubes is less than 400 nm, suggesting that the sample can hardly absorb visible light, while pure Bi_2O_3 has obvious absorption edge in the visible region. Compared to TiO_2, TB2 exhibits an obvious red-shift absorption and an enhanced visible-light response because of the coupling between TiO_2 and Bi_2O_3 [30,31]. In contrast to TiO_2 and TB2, ATB2 shows much higher absorption intensity in the visible light range, which is mainly attributed to the LSPR excitation in Ag nanoparticles [24,46,47,48,49]. The estimated band gaps of samples are shown in Fig. 3(b) according to Tauc plots (see Tauc plot method in SI for details) [35,50]. TB2 heterostructures shortens its bandgap from 3.05 eV to 2.65 eV due to the strong coordination of heterojunction. The ATB2 photocatalyst further shortens its bandgap to 2.40 eV, promoting visible light absorption.

To find out the pathway of carriers transfer, the energy band structures of catalysts need to be determined [51]. The Mott-Schottky curve is used to confirm the type and the flat potential (E_{fp}) of photocatalysts [52]. As shown in Fig. 3(c), the Mott-Schottky curve slopes of TiO_2 and Bi_2O_3 are both positive, implying that they are n-type semiconductors [53]. The E_{fp} (vs Ag/AgCl) of TiO_2 and Bi_2O_3 are − 0.45 eV and − 0.64 eV, respectively, which can be converted into E_{NHE} potential (vs. NHE) according to the Eq. (1) [54,55]:

$$E_{NHE} = E_{fp\cdot} + E^0_{Ag/AgCl} \quad (1)$$

where $E^0_{Ag/AgCl} = 0.210$ eV [56]. The E_{NHE} of TiO_2 and Bi_2O_3 are calculated to be about − 0.24 eV and − 0.43 eV, respectively. It is known that the conduction band (CB) bottom of many n-type semiconductors is more negative by ~ − 0.10 eV than the E_{NHE} [35,55]. Thus, the CB positions of TiO_2 and Bi_2O_3 are − 0.34 eV and − 0.53 eV (vs. NHE). The valence band (VB) positions of TiO_2 and Bi_2O_3 are 2.71 eV and 2.09 eV (vs. NHE), respectively. Moreover, with the introduction of Bi_2O_3 and Ag NPs, the E_{fp} of TB2 and ATB2 gradually shifts to negative potential with a smaller slope, suggesting that TB2 and ATB2 have a higher carrier density and much faster carrier transfer [53,57,58].

In order to study the charge transfer resistance of the as-synthesized photocatalysts, EIS measurement is carried out, as depicted in Fig. 3(d). ATB2 manifests the smallest impedance arc radius, implying that ATB2 has the lowest charge transfer resistance and most valid mobility. This may further improve the catalytic activity. The transient photocurrent response and fluorescence emission spectra (PL) were measured to investigate the light response and charge separation of the prepared TiO_2, TB2, and ATB2 photocatalysts. As observed in Fig. 3(e), the photocurrent intensity of ATB2 is a 1.74-fold and 3.60-fold increase than those of TB2 and TiO_2, respectively, that we attribute to the strong

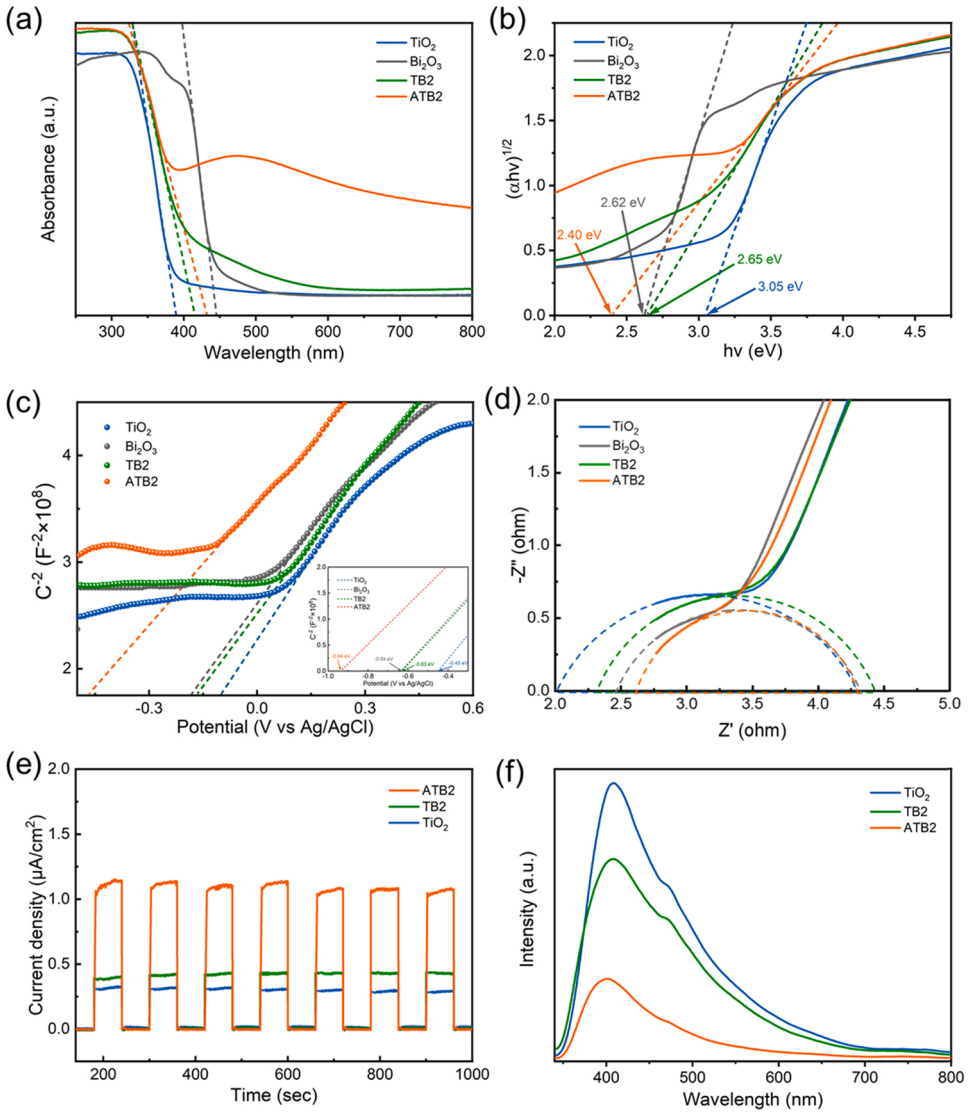

Fig. 3. (a) UV–Vis diffuse reflectance spectra. (b) Estimated band gaps of samples by Tauc plots. (c) Mott-Schottky plots of TiO_2, Bi_2O_3, TB2, and ATB2. (d) The EIS Nyquist plots of TiO_2, Bi_2O_3, TB2, and ATB2. (e)Transient photocurrent responses and (f) fluorescence emission spectra of pure TiO_2, TB2, and ATB2.

spectral absorption as shown in Fig. 3(a) [59,65]. Moreover, ATB2 photocatalysts display the lowest fluorescence intensity compared to TiO_2 and TB2 in Fig. 3(f) because the recombination of charge carriers is significantly inhibited in ATB2. Based on the above analysis, the intense light absorption and the effective charge separation of photogenerated carriers lay a good foundation for applications with enhanced photocatalytic performance.

The photocatalytic performance of the as-prepared materials was evaluated by degrading RhB (10 mg/L) under a 300 W xenon lamp. Pure TiO_2 and Ag@TiO_2 (AT) are used as reference photocatalysts. As illustrated in Fig. 4(a), all photocatalysts systems reach the adsorption-desorption equilibrium before illumination. In the dark reaction stage, ATB2 has a pronounced RhB adsorption effect, meaning that there may be more active adsorption sites on ATB2 than in other samples. After irradiation for 90 min, 100% of RhB can be removed by using ATB2, while only 41% is degraded in the case of pure TiO_2. The higher performance of ATB2 is due to the synergy in Bi_2O_3-TiO_2 heterojunction and Ag nanoparticles. The photocatalytic performance of TB2 is also higher than that of TB1 and TB3 (Fig. S3(a) in SI). According to the optical and electrochemical measurements in Fig. 3(a) and (d–f), the excellent light absorption, low charge transfer resistance, and the effective charge separation of ATB2 make a much higher degradation efficiency possible.

The degradation kinetics of RhB is fitted to quantitatively compare the catalytic activity as shown in Fig. 4(b) (Langmuir Hinshelwood model [61,62,63] in SI). The specific values are presented in the histogram (Fig. S3(b) in SI). The photodegradation rate of TB2 and ATB2 are 1.22-fold and 4.94-fold higher than that of pure TiO_2, highlighting a remarkable photocatalytic activity. To achieve the goal of cutting costs, the reusability and chemical stability of ATB2 photocatalyst is evaluated through four consecutive RhB degradation cycles under full-spectrum light irradiation. After each photodegrading test, the photocatalyst is centrifuged, rinsed with deionized water, dried at 60 °C, and then reused for the next run. Fig. 4(c) revealed that the removal of RhB can still reach up to 99% even after the fourth cycle, indicating the excellent photocatalytic activity and recyclability of the sample in water pollution treatment. Moreover, ATB2 is also suitable for the degradation of other types of dyes such as methyl orange (MO) as shown in Fig. S4 (see in SI for details).

The applicability in a practical scenario for as-prepared photocatalysts is very important. The same photocatalytic systems are used to study the degradation performance of TCH as shown in Fig. 4(d). All samples achieved adsorption-desorption equilibrium before the photodegradation process. After 120 min of degradation, the removal

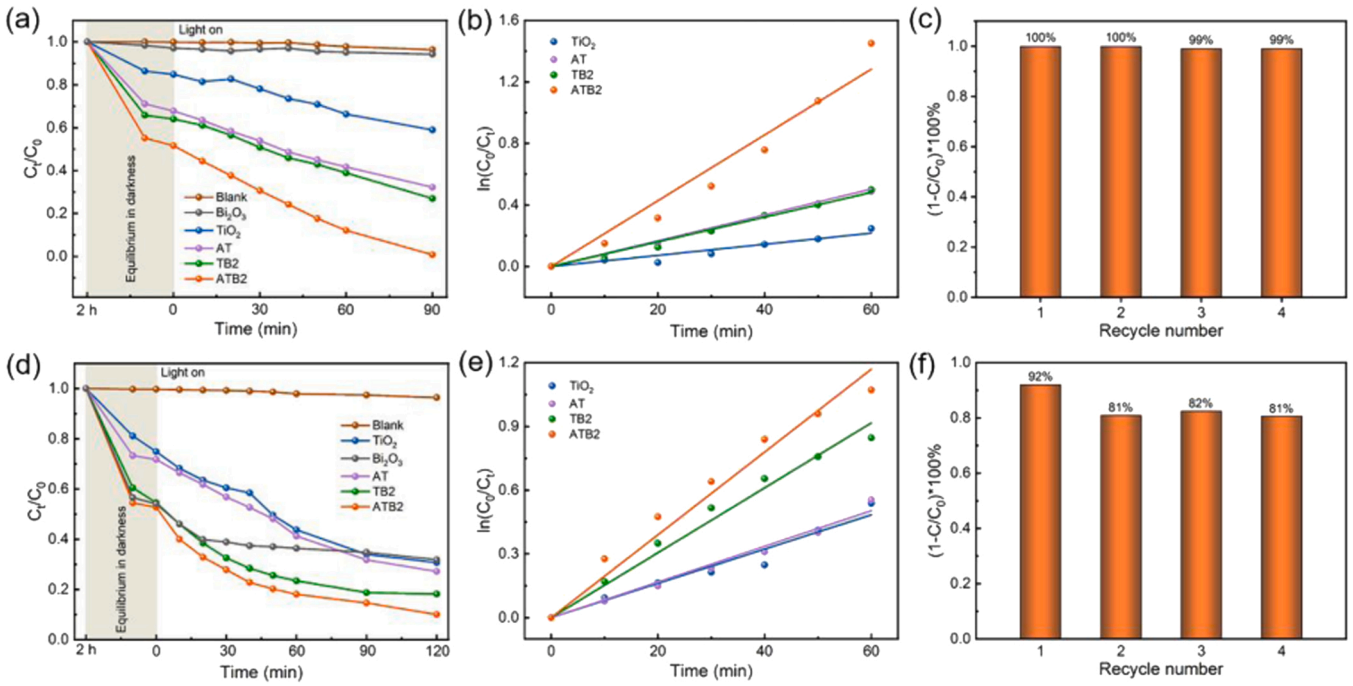

Fig. 4. RhB (a) and TCH (d) removal in the blank and photocatalytic systems. Pseudo-first-order reaction kinetics curves of RHB (b) and TCH (e) degradation in photocatalytic systems. Cycling tests for the degradation of RHB (c) and TCH (f) by using ATB2 photocatalysts.

efficiency of TCH reached 92.0% in the case of ATB2 while only ca. 69.3% was reached with pure TiO_2. As depicted in Fig. 4(e) and Fig. S3 (c), the k_1 value of ATB2 is also higher than that of pure TiO_2 and Ag@TiO_2, reflecting the fast photocatalytic rate and outstanding activity of ATB2. A comparison between this study and other researches is listed in Table S2. As can be seen in Table S2, the removal efficiency of organic pollutants by using as-prepared ATB2 in this work is equivalent to or even better than that of other catalytic systems reported in previous literatures. As illustrated in Fig. 4(f) for photocatalysts reusability, the removal efficiency decreases slightly after the first cycle but maintains stability over the last three degradation cycles. The photocatalytic activity results show that ATB2 has stable photocatalytic recyclability performance under full-spectrum light irradiation. In addition, to further investigate the stability of ATB2 composites, the used ATB2 composites after four cycle tests were investigated by XRD. As shown in Fig. S5, XRD patterns of ATB2 composites before and after cycle tests are almost the same, suggesting that there is barely change in the crystalline phase of ATB2 composites. Thus, Ag@Bi_2O_3-TiO_2 composites show great stability and recyclability for eliminating organic contaminants.

To reveal the photocatalytic degradation mechanism of Ag@Bi_2O_3-TiO_2, the main oxide species are determined by active substance capture experiments; the results are illustrated in Fig. 5(a) and Fig. S6(a, b). Herein, EDTA-2Na, P-BQ, and TBA are utilized to scavenge photogenerated h^+, $\bullet O_2^-$, and •OH, respectively [30,61,64]. When EDTA-2Na is added to the reaction system, a sharp decrease in TCH degradation efficiency compared to the control without free radical scavenger is observed. The results reveal that h^+ plays a significant role and $\bullet O_2^-$ plays a relatively minor role in TCH photodegradation.

Based on the above results, a reasonable mechanism for the enhanced photoactivity of Ag@Bi_2O_3-TiO_2 heterostructure is proposed. The band structure (TiO_2, Bi_2O_3) and standard redox potential (H_2O/•OH, OH^-/•OH, O_2/$\bullet O_2^-$) [60,65,66,67] are illustrated in Fig. 5(b), and thus an S-scheme heterojunction is formed. When Bi_2O_3 and TiO_2 are initially in close contact, electrons in the Bi_2O_3 spontaneously diffuse to TiO_2, creating an electron depletion layer and electron accumulation layer near the Bi_2O_3 and TiO_2 interface, respectively. An internal electric field (IEF) directing from Bi_2O_3 to TiO_2 is formed, which prevents the electrons from flowing from the CB of Bi_2O_3 to that of TiO_2 and restrains holes from the VB of TiO_2 flowing to that of Bi_2O_3. Meanwhile, the electrons of TiO_2 and the holes of Bi_2O_3 drift towards each other and then recombine under the action of the IEF. Consequently, the electrons in Bi_2O_3 and the holes in TiO_2 with strong redox ability remain and are

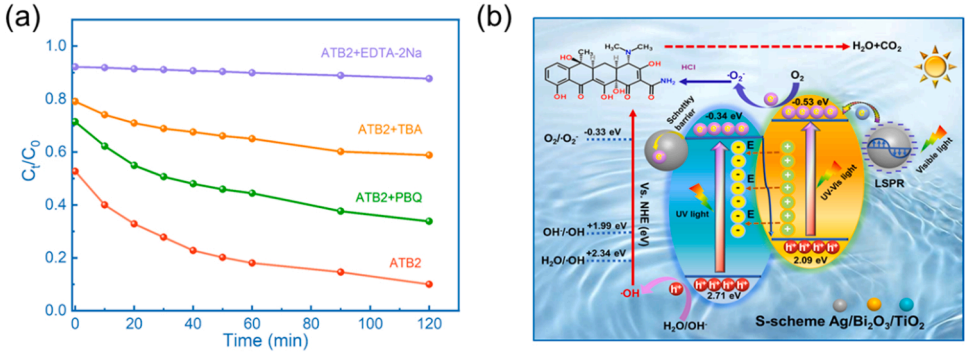

Fig. 5. (a) Trapping experiments of active species over ATB2 photocatalysts for - TCH degradation with the addition of different scavengers. (b) Illustration of the enhanced -photodegradation of TCH over Ag@Bi_2O_3-TiO_2 photocatalysts under full-spectrum light irradiation.

spatially separated. The h^+ in the VB of TiO_2 mainly interacts with TCH molecules directly, and some of them react with OH^- or H_2O to generate •OH radicals based on the potential of H_2O/•OH and OH^-/•OH. The electrons in CB of Bi_2O_3 can be trapped by dissolved oxygen to generate $•O_2^-$ radical species. In addition, under UV light illumination, the Schottky barrier can be formed [68] at the interface between Ag and TiO_2 due to electron migration, which further reduces the recombination of photogenerated carriers in TiO_2. Thus, the number of h^+ in the VB of TiO_2 is further increased. Furthermore, under visible light irradiation, hot electrons produced by the LSPR excitation of Ag NPs can be transferred to the CB of Bi_2O_3 [69,70]. In this way, the number of e^- involved in $•O_2^-$ formation is also increased. All the characteristics mentioned above endow Ag@Bi_2O_3-TiO_2 heterogeneous photocatalysts with excellent photocatalytic activity.

4. Conclusions

In this work, Ag@Bi_2O_3-TiO_2 photocatalysts were obtained by using a strategy based on sacrificial templates and photoreduction. S-scheme heterojunction between Bi_2O_3 and TiO_2 made electrons in Bi_2O_3 and the holes in TiO_2 with strong redox ability remain, which was beneficial to the photocatalytic reaction. The modification with Ag NPs further boosted the photocatalytic efficiency due to the Schottky barrier between Ag and heterostructures and the LSPR effect of Ag NPs, improving the separation of electron-hole pairs and enhancing spectral absorption. Consequently, Ag@Bi_2O_3-TiO_2 photocatalysts showed high removal efficiency of 100% and 92% for RhB and TCH, respectively. Furthermore, Ag@Bi_2O_3-TiO_2 photocatalysts showed stable photocatalytic recyclability under full-spectrum light irradiation. This work offers a facile strategy to prepare nanoparticles modified heterogeneous nanotubular photocatalysts with high photocatalytic properties to degrade organic contaminants efficiently.

CRediT authorship contribution statement

Yan Wang: Methodology, Writing – original draft. **Shengzhe Zhao:** Resources. **Yi Yang**: Visualization. **Yun Lu:** Validation, Project administration. **Raul D. Rodriguez:** Writing – review & editing. **Anya Lipovka:** Formal analysis. **Honglan Huang:** Investigation. **Jinju Chen:** Conceptualization, Supervision.

Declaration of Competing Interest

The authors declare that they have no known competing financial interests or personal relationships that could have appeared to influence the work reported in this paper.

Acknowledgements

This work is financially supported by National Natural Science Foundation of China (Grant No. 52073265, China) and TPU Development Program (Russia).

Appendix A. Supporting information

Supplementary data associated with this article can be found in the online version at doi:10.1016/j.colsurfa.2022.129233.

References

[1] Y. Zhou, T. Cai, S. Liu, Y. Liu, H. Chen, Z. Li, J. Du, Z. Lei, H. Peng, N-doped magnetic three-dimensional carbon microspheres@TiO_2 with a porous architecture for enhanced degradation of tetracycline and methyl orange via adsorption/photocatalysis synergy, Chem. Eng. J. 411 (2021), 128615.
[2] C.H. Nguyen, C.-C. Fu, R.-S. Juang, Degradation of methylene blue and methyl orange by palladium-doped TiO_2 photocatalysis for water reuse: efficiency and degradation pathways, J. Clean. Prod. 202 (2018) 413–427.
[3] J.H. Weisburger, Comments on the history and importance of aromatic and heterocyclic amines in public health, Mutat. Res. 506 (7) (2002) 9–20.
[4] M.S. Tsuboy, J. Angeli, M.S. Mantovani, S. Knasmüller, G.A. Umbuzeiro, L. R. Ribeiro, Genotoxic, mutagenic and cytotoxic effects of the commercial dye CI Disperse Blue 291 in the human hepatic cell line HepG2, Toxicol. Vitr. 21 (8) (2007) 1650–1655.
[5] Y. Zhang, A. Yu, L. Jiang, C. Geng, J. Cao, L. Jiang, L. Zhong, The role of oxidative stress in Sudan IV-induced DNA damage in human liver-derived HepG2 cells, Environ. Toxicol. 26 (3) (2011) 292–299.
[6] J. Chen, G.G. Ying, W.J. Deng, Antibiotic residues in food: extraction, analysis, and human health concerns, J. Agric. Food Chem. 67 (27) (2019) 7569–7586.
[7] T. Hagan, M. Cortese, N. Rouphael, C. Boudreau, C. Linde, M.S. Maddur, J. Das, H. Wang, J. Guthmiller, N.Y. Zheng, M. Huang, A.A. Uphadhyay, L. Gardinassi, C. Petitdemange, M.P. McCullough, S.J. Johnson, K. Gill, B. Cervasi, J. Zou, A. Bretin, M. Hahn, A.T. Gewirtz, S.E. Bosinger, P.C. Wilson, S. Li, G. Alter, S. Khurana, H. Golding, B. Pulendran, Antibiotics-driven gut microbiome perturbation alters immunity to vaccines in humans, Cell 178 (6) (2019) 1313–1328.
[8] X. Liu, Y. Yang, H. Li, Z. Yang, Y. Fang, Visible light degradation of tetracycline using oxygen-rich titanium dioxide nanosheets decorated by carbon quantum dots, Chem. Eng. J. 408 (2021), 127259.
[9] P.E. Stackelberg, J. Gibs, E.T. Furlong, M.T. Meyer, S.D. Zaugg, R.L. Lippincott, Efficiency of conventional drinking-water-treatment processes in removal of pharmaceuticals and other organic compounds, Sci. Total Environ. 377 (2–3) (2007) 255–272.
[10] Y.W. Yang, T.L. Zhou, Q.C. Qiao, Experimental study of wastewater treatment of reactive dye by phys-chemistry method, J. China Univ. Min. Technol. 17 (1) (2007) 96–100.
[11] L. Qin, R.Y. Gao, L.I. Guo-Xue, X.W. Liu, L.I. Hong, Y. Liu, L. Wang, Decomposition effect of additive of composite microbial system on cellulose and chlortetracycline in composting, J. Agro-Environ. Sci. 28 (4) (2009) 820–823.
[12] Y.F. Wang, B.Y. Gao, Q.Y. Yue, Y. Wang, Z.L. Yang, Removal of acid and direct dye by epichlorohydrin-dimethylamine: flocculation performance and floc aggregation properties, Bioresour. Technol. 113 (2012) 265–271.
[13] M.J. Dietrich, T.L. Randall, P.J. Canney, Wet air oxidation of hazardous organics in wastewater, Environ. Prog. Sustain. Energy 4 (3) (2010) 171–177.
[14] H. Tong, S. Ouyang, Y. Bi, N. Umezawa, M. Oshikiri, J. Ye, Nano-photocatalytic materials: possibilities and challenges, Adv. Mater. 24 (2) (2012) 229–251.
[15] S. Xiong, Y. Yu, P. Wang, M. Liu, S. Chen, X. Yin, L. Wang, L. Wang, Growth of AgBr/Ag_3PO_4 heterojunction on chitosan fibers for degrading organic pollutants, Adv. Fiber Mater. 2 (5) (2020) 246–255.
[16] Y. Sun, J.B. Mwandeje, L.M. Wangatia, F. Zabihi, J. Nedeljković, S. Yang, Enhanced photocatalytic performance of surface-modified TiO_2 nanofibers with rhodizonic acid, Adv. Fiber Mater. 2 (2020) 118–122.
[17] Y. Zhang, A. Sun, M. Xiong, K.M. Daniel, J. Liu, Z. Chen, M. Li, L. Zhang, TiO_2/BiOI p-n junction-decorated carbon fibers as weavable photocatalyst with UV–vis photoresponsive for efficiently degrading various pollutants, Chem. Eng. J. 415 (6402) (2021), 129019.
[18] G. Duoerkun, Y. Zhang, Z. Shi, X. Shen, W. Cao, T. Liu, J. Liu, Q. Chen, L. Zhang, Construction of n-TiO_2/p-Ag_2O junction on carbon fiber cloth with Vis-NIR photoresponse as a filter-membrane-shaped photocatalyst, Adv. Fiber Mater. 2 (1) (2020) 13–23.
[19] Q. Zou, H. Li, Y. Yang, Y. Miao, Y. Huo, Bi_2O_3/TiO_2 photocatalytic film coated on floated glass balls for efficient removal of organic pollutant, Appl. Surf. Sci. 467–468 (2019) 354–360.
[20] Y. Huang, Y. Wei, J. Wang, D. Luo, L. Fan, J. Wu, Controllable fabrication of Bi_2O_3/TiO_2 heterojunction with excellent visible-light responsive photocatalytic performance, Appl. Surf. Sci. 423 (2017) 119–130.
[21] J. Zhu, S. Wang, J. Wang, D. Zhang, H. Li, Highly active and durable Bi_2O_3/TiO_2 visible photocatalyst in flower-like spheres with surface-enriched Bi_2O_3 quantum dots, Appl. Catal. B: Environ. 102 (1–2) (2011) 120–125.
[22] A. Nagar, S. Basu, Deciphering the role of β-phase Bi_2O_3 nanorods incorporated on g-C_3N_4 nanosheets for efficient pollutant removal, J. Phys. Chem. Solids 164 (2022), 110625.
[23] A. Nagar, S. Basu, Fabrication of 3D porous peony flower-like β-Bi_2O_3/BiOCl heterostructure for synergistically boosting the visible-light-driven degradation of organic pollutants, Environ. Technol. Innov. 24 (2021), 101956.
[24] J. Wang, H. Liang, C. Zhang, B. Jin, Y. Men, Bi_2WO_{6-x} nanosheets with tunable Bi quantum dots and oxygen vacancies for photocatalytic selective oxidation of alcohols[J], Appl. Catal. B: Environ. 256 (2019), 117874.
[25] D. Monga, S. Basu, Enhanced photocatalytic degradation of industrial dye by g-C_3N_4/TiO_2 nanocomposite: role of shape of TiO_2, Adv. Powder Technol. 30 (5) (2019) 1089–1098.
[26] D. Wang, X. Yu, Q. Feng, X. Lin, Y. Huang, X. Huang, X. Li, K. Chen, B. Zhao, Z. Zhang, In-situ growth of β-Bi_2O_3 nanosheets on g-C_3N_4 to construct direct Z-scheme heterojunction with enhanced photocatalytic activities, J. Alloy. Compd. 859 (2021), 157795.
[27] Z. Liang, Y. Cao, Y. Li, J. Xie, N. Guo, D. Jia, Solid-state chemical synthesis of rod-like fluorine-doped β-Bi_2O_3 and their enhanced photocatalytic property under visible light, Appl. Surf. Sci. 390 (2016) 78–85.
[28] Y. Li, F. Yang, Y. Yu, Enhanced photocatalytic activity of α-Bi2O3 with high electron-hole mobility by codoping approach: a first-principles study, Appl. Surf. Sci. 358 (2015) 449–456.
[29] B. Lou, C. Chen, J. Liu, S. Zou, L. Xiao, J. Fan, Selectively depositing Bi_2O_3 quantum dots on TiO_2 nanotubes for efficient visible-light-driven photocatalysis, Mater. Lett. 288 (2021), 129413.

[30] T. Tang, Z. Yin, J. Chen, S. Zhang, W. Sheng, W. Wei, Y. Xiao, Q. Shi, S. Cao, Novel p-n heterojunction Bi_2O_3/Ti^{3+}-TiO_2 photocatalyst enables the complete removal of tetracyclines under visible light, Chem. Eng. J. 417 (2021), 128058.
[31] M.N. Gómez-Cerezo, M.J. Muñoz-Batista, D. Tudela, M. Fernández-García, A. Kubacka, Composite Bi_2O_3-TiO_2 catalysts for toluene photo-degradation: ultraviolet and visible light performances, Appl. Catal. B: Environ. 156–157 (2014) 307–313.
[32] J. Chen, T. Tang, W. Feng, X. Liu, Z. Yin, X. Zhang, J. Chen, S. Cao, Large-scale synthesis of p-n heterojunction Bi_2O_3/TiO_2 nanostructures as photocatalysts for removal of antibiotics under visible light, ACS Appl. Nano Mater. 5 (1) (2022) 1296–1307.
[33] A. Bazmeh, A. Fatehizadeh, B. Bina, B. Shoshtari-Yeganeh, Mechanism of oxidative decomposition of direct red 89 by Bi_2O_3/TiO_2 composite under visible light irradiation: effect of co-existing cations and anions and artificial neural network modeling of key factor, Desalin. Water Treat. 212 (2021) 333–346.
[34] S. You, Y. Hu, X. Liu, C. Wei, Synergetic removal of Pb(II) and dibutyl phthalate mixed pollutants on Bi_2O_3-TiO_2 composite photocatalyst under visible light, Appl. Catal. B: Environ. 232 (2018) 288–298.
[35] X. Yu, J. Huang, J. Zhao, S. Liu, D. Xiang, Y. Tang, J. Li, Q. Guo, X. Ma, J. Zhao, Efficient visible light photocatalytic antibiotic elimination performance induced by nanostructured $Ag/AgCl@Ti^{3+}$-TiO_2 mesocrystals, Chem. Eng. J. 403 (2021), 126359.
[36] J. Wang, L. Jiang, F. Liu, M. Jia, M. Liu, J. Li, Y. Lai, Enhanced photoelectrochemical degradation of tetracycline hydrochloride with FeOOH and Au nanoparticles decorated WO_3, Chem. Eng. J. 407 (127195) (2021).
[37] N. Kaur, A. Verma, I. Thakur, S. Basu, In-situ dual effect of Ag-Fe-TiO_2 composite for the photocatalytic degradation of Ciprofloxacin in aqueous solution, Chemosphere 276 (2021), 130180.
[38] P. Wang, C. Peng, M. Yang, Ag decorated 3D urchin-like TiO_2 microstructures synthesized via a one-step solvothermal method and their photocatalytic activity, J. Alloy. Compd. 648 (2015) 22–28.
[39] S. Zhao, J. Chen, Y. Liu, Y. Jiang, C. Jiang, Z. Yin, Y. Xiao, S. Cao, Silver nanoparticles confined in shell-in-shell hollow TiO_2 manifesting efficiently photocatalytic activity and stability, Chem. Eng. J. 367 (2019) 249–259.
[40] X. Li, Y. Jin, Z. Dou, S. Zhou, Q. Zhang, N. Bao, Rational design of Z-scheme $Bi_{12}O_{17}Cl_2$/plasmonic Ag/anoxic TiO_2 composites for efficient visible light photocatalysis, Powder Technol. 384 (2021) 342–352.
[41] Lee, S.K.; Yoon, S.H.; Chung, I.; Hartwig, A.; Kim, B.K., Handbook of X-ray Photoelectron Spectroscopy. 2011.
[42] X. Zheng, D. Li, X. Li, J. Chen, C. Cao, J. Fang, J. Wang, Y. He, Y. Zheng, Construction of ZnO/TiO_2 photonic crystal heterostructures for enhanced photocatalytic properties, Appl. Catal. B: Environ. 168–169 (2015) 408–415.
[43] M.C. Biesinger, L.W.M. Lau, A.R. Gerson, R.S.C. Smart, Resolving surface chemical states in XPS analysis of first row transition metals, oxides and hydroxides: Sc, Ti, V, Cu and Zn, Appl. Surf. Sci. 257 (3) (2010) 887–898.
[44] V. Bilovol, S. Ferrari, D. Derewnicka, F.D. Saccone, XANES and XPS study of electronic structure of Ti-enriched Nd–Fe–B ribbons, Mater. Chem. Phys. 146 (3) (2014) 269–276.
[45] H. Lu, Q. Hao, T. Chen, L. Zhang, D. Chen, C. Ma, W. Yao, Y. Zhu, A high-performance Bi_2O_3/Bi_2SiO_5 p-n heterojunction photocatalyst induced by phase transition of Bi_2O_3, Appl. Catal. B: Environ. 237 (2018) 59–67.
[46] P. Wang, B. Huang, X. Qin, X. Zhang, Y. Dai, J. Wei, M.H. Whangbo, Ag@AgCl: a highly efficient and stable photocatalyst active under visible light, Angew. Chem. Int. Ed. Engl. 47 (41) (2008) 7931–7933.
[47] G. Dai, B. Huang, J. Yu, Fabrication and characterization of visible-light-driven plasmonic photocatalyst Ag/AgCl/ TiO2 nanotube arrays, J. Phys. Chem. C 113 (37) (2009) 16394–16401.
[48] H. Xu, H. Li, J. Xia, S. Yin, Z. Luo, L. Liu, L. Xu, One-pot synthesis of visible-light-driven plasmonic photocatalyst Ag/AgCl in ionic liquid, ACS Appl. Mater. Interfaces 3 (1) (2011) 22–29.
[49] Z. Hao, G. Wang, C. Da, X. Lv, J. Li, Tuning photoelectrochemical performances of Ag-TiO_2 nanocomposites via reduction/oxidation of Ag, Chem. Mater. 77 (1) (2008) 87–95.
[50] S. Tan, Z. Xing, J. Zhang, Z. Li, X. Wu, J. Cui, J. Kuang, Q. Zhu, W. Zhou, Ti^{3+}-TiO_2/g-C_3N_4 mesostructured nanosheets heterojunctions as efficient visible-light-driven photocatalysts, J. Catal. 357 (2018) 90–99.
[51] R. Beranek, Photo)electrochemical methods for the determination of the band edge positions of TiO_2-Based nanomaterials, Adv. Phys. Chem. 2011 (2011) 1–20.
[52] K. Gelderman, L. Lee, S.W. Donne, Flat-band potential of a semiconductor: using the Mott Schottky equation, J. Chem. Educ. 84 (4) (2007) 685–688.
[53] H. Liu, D. Chen, Z. Wang, H. Jing, R. Zhang, Microwave-assisted molten-salt rapid synthesis of isotype triazine-/heptazine based g-C_3N_4 heterojunctions with highly enhanced photocatalytic hydrogen evolution performance, Appl. Catal. B: Environ. 203 (2017) 300–313.
[54] Y. Surendranath, D.A. Lutterman, Y. Liu, D.G. Nocera, Nucleation, growth, and repair of a cobalt-based oxygen evolving catalyst, J. Am. Chem. Soc. 134 (14) (2012) 6326–6336.
[55] J. Wang, Y. Yu, L. Zhang, Highly efficient photocatalytic removal of sodium pentachlorophenate with Bi_3O_4Br under visible light, Appl. Catal. B: Environ. 136–137 (2013) 112–121.
[56] J. Andersen, L.L. Madsen, N. Bonander, P. Møller, J. Ulstrup, Dynamics of Pseudomonas aeruginosa azurin and its Cys3Ser mutant at single-crystal gold surfaces investigated by cyclic voltammetry and atomic force microscopy, Electrochim. Acta 42 (19) (1997) 2889–2897.
[57] S. Bai, J. Liu, M. Cui, R. Luo, J. He, A. Chen, Two-step electrodeposition to fabricate the p–n heterojunction of a $Cu_2O/BiVO_4$ photoanode for the enhancement of photoelectrochemical water splitting, Dalton Trans. 47 (19) (2018) 6763–6771.
[58] J. Ma, Q. Wang, L. Li, X. Zong, H. Sun, R. Tao, X. Fan, Fe_2O_3 nanorods/CuO nanoparticles p-n heterojunction photoanode: effective charge separation and enhanced photoelectrochemical properties, J. Colloid Interface Sci. 602 (2021) 32–42.
[59] Y. Wen, H. Ding, Y. Shan, Preparation and visible light photocatalytic activity of Ag/TiO_2/graphene nanocomposite, Nanoscale 3 (10) (2011) 4411–4417.
[60] D. Zhang, G. Tan, M. Wang, B. Li, A. Xia, The enhanced photocatalytic activity of Ag-OVs-(001) BiOCl by separating secondary excitons under double SPR effects, Appl. Surf. Sci. 526 (2020), 146689.
[61] C. Tian, H. Zhao, H. Sun, K. Xiao, P. Keung Wong, Enhanced adsorption and photocatalytic activities of ultrathin graphitic carbon nitride nanosheets: Kinetics and mechanism, Chem. Eng. J. 381 (2020), 122760.
[62] F. Zhou, C. Yan, T. Liang, Q. Sun, H. Wang, Photocatalytic degradation of Orange G using sepiolite-TiO_2 nanocomposites: optimization of physicochemical parameters and kinetics studies, Chem. Eng. Sci. 183 (2018) 231–239.
[63] R.A. Doong, S.M. Chang, C.W. Tsai, Enhanced photoactivity of Cu-deposited titanate nanotubes for removal of bisphenol A, Appl. Catal. B: Environ. 129 (2013) 48–55.
[64] J. Cao, B. Xu, B. Luo, H. Lin, S. Chen, Novel BiOI/BiOBr heterojunction photocatalysts with enhanced visible light photocatalytic properties, Catal. Commun. 13 (1) (2011) 63–68.
[65] R. Hao, G. Wang, H. Tang, L. Sun, D. Han, Template-free preparation of macro/mesoporous g-C_3N_4/TiO_2 heterojunction photocatalysts with enhanced visible light photocatalytic activity, Appl. Catal. B Environ. 187 (2016) 47–58.
[66] H. Wang, B. Liao, T. Lu, Y. Ai, G. Liu, Enhanced visible-light photocatalytic degradation of tetracycline by a novel hollow BiOCl@CeO_2 heterostructured microspheres: structural characterization and reaction mechanism, J. Hazard. Mater. 385 (2020), 121552.
[67] X. Li, Y. Jin, Z. Dou, S. Zhou, Q. Zhang, N. Bao, Rational design of Z-scheme $Bi_{12}O_{17}Cl_2$/plasmonic Ag/anoxic TiO_2 composites for efficient visible light photocatalysis, Powder Technol. 384 (2021) 342–352.
[68] L. Gomathi Devi, R. Kavitha, A review on plasmonic metal TiO_2 composite for generation, trapping, storing and dynamic vectorial transfer of photogenerated electrons across the Schottky junction in a photocatalytic system, Appl. Surf. Sci. 360 (2016) 601–622.
[69] C. Clavero, Plasmon-induced hot-electron generation at nanoparticle/metal-oxide interfaces for photovoltaic and photocatalytic devices, Nat. Photonics 8 (2) (2014) 95–103.
[70] S. Mukherjee, F. Libisch, N. Large, O. Neumann, L.V. Brown, J. Cheng, J.B. Lassiter, E.A. Carter, P. Nordlander, N.J. Halas, Hot electrons do the impossible: plasmon-induced dissociation of H_2 on Au, Nano Lett. 13 (1) (2013) 240–247.